Comparative Concerns with Li-Ion Battery Cathode Materials

S Nagaveni[1], Ch Venkateswarlu[2], K V Prasanna Kumari[3]

[1]Associate Professor in Physics , CMR Institute of Technology , Hyderabad,Telangana India.

[2]Assistant Professor in Physics , CMR Institute of Technology , Hyderabad,Telangana India.

[3]Assistant Professor in Physics, Sphoorthy Engineering College, Hyderabad, Telangana, India.

Email:nagaveni.sangisetti@gmail.com

Abstract:

Following an overview of lithium insertion compounds and Li-ion cell principles, we compare the physical and electrochemical characteristics of the positive electrodes found in Li-ion batteries (LIBs). Three types of electrode materials include several kinds of lattices, including spinel frameworks, layered transition-metal oxides, and olivine, based on the dimensionality of the Li+ ion motion within them. With a focus on synthesis challenges, electrochemical stability, faradaic performance, and security concerns, their benefits and drawbacks are contrasted.

Keywords: phase diagram, safety, Li-ion batteries, and lithium-insertion compounds

1. Introduction :

Lithium-ion batteries (LIBs) have been one of the most promising chemical-electrical energy converters (rechargeable or secondary sources) for powering electronic devices including laptop computers, cell phones, cameras, and more for the past thirty years. The financial performance of LIBs based on Lithium cobaltate ($LiCoO_2$) and carbon, a non-aqueous electrolyte, showed tremendous promise as being Soon, personal gadgets will use the first rechargeable battery technology [1]. These days, this technology is used in environmentally friendly transportation systems including hybrid electric vehicles (HEVs) and electric cars (EVs). Higher demand for highly functionalized applications is always accompanied by greater safety, superior charge-discharge cycling performance, increased energy density, and power density.

The active element of the positive electrode, which is also the most costly component, is a crucial component that restricts the batteries' performance. Since 1980, Goodenough has consistently worked to suggest and investigate oxide compounds based on transition-metal (TM) element that focuses on substances that crystallize in configurations that allow for high Li+ ion mobility for energy transfer during the redox process. In 1980, significant advancements were made for the $LiMn_2O_4$ spinels [3,4], $LiCoO_2$ layered structure [2], and the $LiMPO_4$ (M = Fe, Mn, etc.) olivine family [5] were discovered in 1986 and 1997, respectively. All of these materials have been thoroughly researched and successfully used in the production of commercial Li-ion

batteries in a short period of time. Materials in layers are utilized as cathodes for high-energy systems [6,7], whereas olivines and spinel oxides are taken into consideration for high-power Li-ion batteries due to their extended lifespan and low cost, respectively [8,9]. These lithium-insertion compounds must, however, meet certain requirements, including toxicity, cost, safety, capacity, rate capability, and chemical stability. At a potential >3.4 V vs. Li0/Li^+, all of them, however, achieve a theoretical specific capacity >140 mA g^{-1}. The electrochemical characteristics of the three groups of insertion compounds are presented in Table 1.

Table 1 : lists the electrochemical properties of the three insertion compound types.

Framework	Compound	Specific capacity [a] (mAh g^{-1})	Average potential (V *vs.* Li^0/Li^+)
Layered	$LiCoO_2$	272 (140)	4.2
	$LiNi_{1/3}Mn_{1/3}Co_{1/3}O_2$	272 (200)	4.0
Spinel	$LiMn_2O_4$	148 (120)	4.1
	$LiMn_{3/2}Ni_{1/2}O_4$	148 (120)	4.7
Olivine	$LiFePO_4$	170 (160)	3.45
	$LiFe_{1/2}Mn_{1/2}PO_4$	170 (160)	3.4/4.1

[a] Value in parenthesis indicates the practical specific capacity of electrode.

The benefits and drawbacks of the positive electrode materials used in Li-ion batteries are discussed in this study. These materials include layered LiCoO2 (LCO), LiNiyMnyCo1−2yO_2 (NMC), spinel $LiMn_2O_4$ (LMO), $LiMn_{1.5}Ni0.5O_4$ (LMN), and olivine $LiFePO_4$ (LFP). Even though thousands of papers have been published,

There aren't many comparison studies of these materials' characteristics as active electrochemical elements given their evolution. From the perspective of Li^+ ion mobility in these three types of lattices, we aim to report on the challenges associated with synthesis, electrochemical stability and performance, and security considerations.

Particular attention is paid to olivine Li(Fe,Mn)PO_4 as an efficient lithium-insertion compound, since it is thought to be the most promising option for the next generation of large-scale Li-ion batteries, not just for usage in EVs or HEVs, but also to address intermittently use energy storage and smart grids for high-power applications.

2. The Cell Potential

The primary factor influencing the chemical potential changes throughout the intercalation process directly affects the battery's open-circuit voltage, including

$$-eV_{oc} = \mu_{Li}(C) - \mu_{Li}(A) = \Delta\mu_e + \Delta\mu_{Li^+} \quad (1)$$

wherein the valence electronic density and the involved occupation of sites by Li^+ ions are conceptually separated from the chemical potential of the exchanged Li^-atoms in anode (A) and cathode (C). electrons' states (DOS). A modified occupation of electronic states results from a redox process within the electrode that compensates for the charge compensation of exchanged Li^+ ions. The classical thermodynamic law provides the potential of an intercalation electrode for a given redox pair, which is thought of as the guest A's solution in the host lattice .

$$V(x) = -\frac{1}{zF}\frac{\partial(\Delta G)}{\partial x} + \text{constant} \quad (2)$$

where x is the composition, z is the number of electrons involved, F is the Faraday's constant, and ΔG is the variance in the system's Gibbs energy. In, V(x) represents the electrode potential as a function of composition x.

Figure:1 The electronic density of states and Fermi energies for an oxide-based electrode (LixNi0.5−yMn1.5−yCr2yO4 spinel material) are depicted schematically. The electrode surface's Li permeable solid electrolyte interface (SEI) layer maintains the overall reversible response.

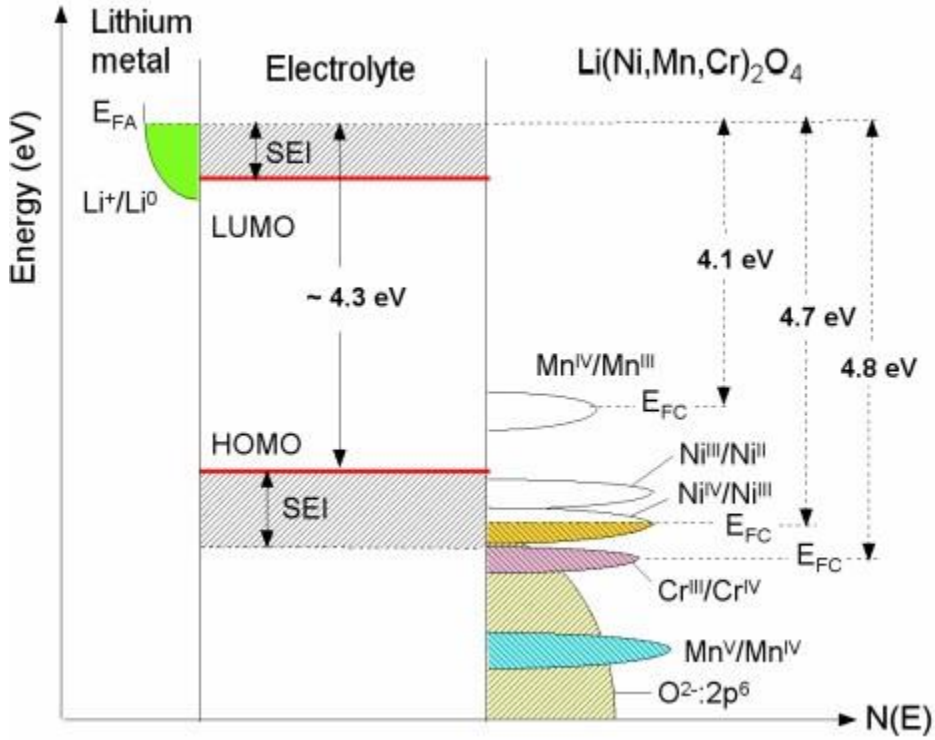

Good enough have talked about the open-circuit energy diagram of a lithium battery (see Figure 1) [11,12]. A localized d-electron manifold present in the active transition-metal cation functions as a redox couple, such as Ni2+/4+ in $LiNi_{1.5}Mn_{0.5}O_4$ (LNM). Redox succession Couples are split apart by an efficient on-site When enhanced by either an intra-atomic exchange splitting or a crystal-field splitting, the Coulomb correlation energy U can be high [13]. Nevertheless, as the cathode material's Fermi energy EFC gets closer to the top of the host's anion p bands, The associated d electrons at EFC may change into band electrons occupying one-electron states as a result of the p-d covalent mixing [11,14]. There is no on-site energy U that separates the one-electron states when there is no crystal-field splitting of the d orbitals at EFC, as occurs for Ni(IV) to Ni(II). There is no step in the battery's voltage. When the host is reduced or oxidized, EFC changes from one formal valence state to another.

3. Electronic Properties and Crystal Structure

Figure 2 displays the crystal structures of the three types of Li-insertion compounds. Their classification is in line with the activation energy and ion diffusion routes that control Li-ion transport in the electrode materials [10]. The two-dimensional $Li[M]O_2$ archetypes with The three-dimensional $Li[X]_2O_4$ with X = Mn, (Mn1−y/2Liy/2) or (Mn3/4Ni1/4), the uni-dimensional $Li[M']PO_4$ with M' = Fe, Mn, Ni, Co, or (FeyMn1−y), and M = Co, Ni, (NixCo1−x) or (NixMnyCoz).

Figure 2: The three lithium-insertion compounds' crystal structures are shown where the Li+ ions can move across the 2-D (layered), 3-D (spinel), and 1-D (olivine) frameworks.

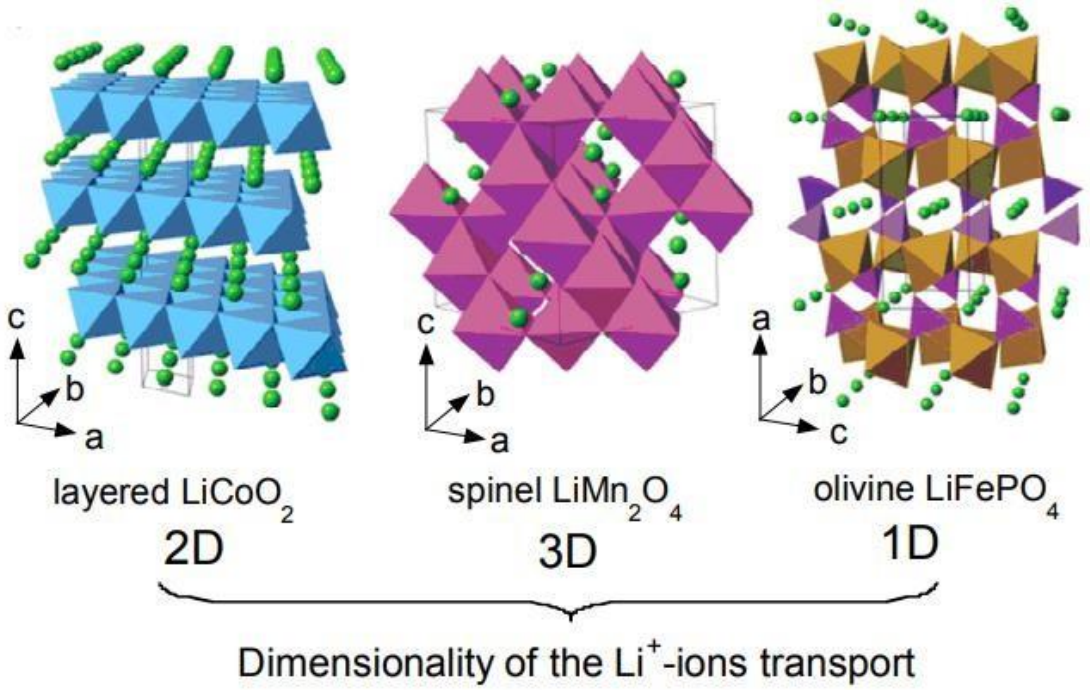

3.1. Compounds in Layers

With the oxygen ions closely packed in a cubic arrangement and the TM and Li ions occupying the octahedral positions of alternate layers with an ABCABC… stacking sequence known as the "O3-type" structure, Li[M]O_2 (M = Co, Ni) oxides are isostructural to the layered α-NaFeO2 (space group R3m, No. 166). (Fig. 2). The cobalt in LiCoO2 is trivalent in the low-spin state (S = 0), or in the electronic configuration $(t_2g)_6$ (eg) 0. With Li in sites 3a, Ni in sites 3b, and O in sites 6c, LCO, on the other hand, adopts the rhombohedral symmetry in the high temperature form. Three formula units are included in the hexagonal setting's unit-cell. A lithium cell's cycling involves the reversible removal of Li^+ ions from and integrated into this framework, as illustrated in Figure 2, to produce or eliminate vacancies within the lithium planes. These vacancies have the ability to arrange the creation of organized Li-vacancy complexes on a triangular lattice of sites or to indirectly cause electronic transitions in LCO. Be aware of the low temperature form (LT-LCO) uses the cubic symmetry spinel lattice (S.G. Fd3m) [15,16]. To maximize charge delocalization and decrease energy, a lithium ordering and stacking sequence that creates an equivalent environment for all Co ions is desired. In $LixCoO_2$, no Co:eg and Li:2s states couple, and the interplanar stacking that produces the greatest number of equivalent Co sites has the lowest energy. This is in line with a propensity for charge delocalization at x = 0.5 to be $Co^{+3/+4}$. Co often exhibits an intermediate oxidation state of +3.5 in $Li_{0.5}CoO_2$, which triggers a change to a monoclinic structure [17]. Even worse, LiCoO2

experiences oxygen release due to the metal ion dissolving in the electrolyte, which gets more crucial when the temperature rises. Therefore, it has been shown that surface modification using metal-oxide coatings such ZrO2, Al_2O_3, TiO_2, etc. is a successful tactic to prevent cathode break down .

$LiNiO_2$ (LNO) has the O3-type-oxygen packing depicted in Figure 2 and is structurally identical to LiCoO2. A high cell voltage of about 4 V, similar to LCO, is provided by the Ni3+/4+ couple with a high lithium chemical potential. Nevertheless, LNO has a few shortcomings: (i) LiNiO2 synthesis is challenging with all the The chemistry of this compound is better illustrated by Li1−zNi1+zO2, which is composed of nickel ions in the Ni^{3+} valence state and distributed in a well ordered phase without any mixing of Li^+ and Ni^{3+} ions in the lithium plane. (ii) The low spin Ni3+:d7 (t2g 6 eg 1) ion is linked to the Jahn-Teller distortion (tetragonal structural distortion). (iii) Phase changes that happen during the charge-discharge process and cannot be reversed. (iv) Safety issues in the charged state and exothermic oxygen emission at high temperatures [20]. $LiNiO_2$ is therefore not a material that shows promise for use in commercial lithium-ion batteries. However, the primary disadvantages of both LiCoO2 and $LiNiO_2$ oxides can be overcome by mixed $LiNi1-yCoyO_2$ phases. For instance, it has been demonstrated that the solid solutions $LiNi_{0.85}Co_{0.15O2}$ and $LiNi_{0.80}Co_{0.15}A_{l0.05}O_2$ have appealing electrochemical characteristics, including good cyclability and a reversible capacity of about 180 m Ah g^{-1} .

3.2. $LiMn_2O_4$ (LMO)

$LiMn_2O_4$ crystallizes in the Fd3m space group (Oh 7 factor group) with the cubic lattice parameter a = 8.239 Å and is a member of the $A[B_2]$ O_4 spinel-type structure. The structure of the cubic spinel $LiMn_2O_4$ is characterized by a nearly perfect cubic close-packed (ccp) sublattice formed by the oxygen ions on the 32e sites and the Mn and Li cations on the 16d and 8a sites, respectively. The Mn ions occupy half of the octahedral interstices, creating a three-dimensional framework of edge-sharing MnO_6 octahedra. At the 16c location, lithium ions are located in tetrahedral sites that have faces in common with four nearby unoccupied octahedral sites (Figure 2). Lithium ions diffuse during insertion/de insertion processes via a three-dimensional network of transport pathways 16c-8a-16c provided by this lattice. The existence of oxygen vacancies discovered by neutron diffraction measurements must be considered in order to comprehend the LMO spinel from the perspective of solid-state chemistry, and this is debatable. For the "oxygen vacancy" phase, two structural models were put forth: vacancy at the excess cations at the interstitial site with the formula $Li^{1+x}Mn^{2+}yO_4$, and oxygen site corresponding to the formula $LiMn_2O_4-\delta$.

3.3. $LiNi_{0.5}Mn_{1.5}O_4$ (LNM)

In LiMn2O4 spinel, 25% Ni has been substituted for Mn because this composition suggests that Mn is in the 4+ valence, avoiding the Jahn-Teller (JT) distortion linked to Mn3+.

Thus, the only cause of the electrochemical activity is the oxidation/reduction of Ni2+ ions, which leads to 2e− per Ni ion transport. According to the cationic sublattice, LiNi0.5Mn1.5O4 crystallizes into two distinct crystallographic structures: the face-centered spinel (S.G. Fd3m), known as "disordered spinel," and the simple cubic phase (S.G. P4332), known as "ordered spinel." Li on 8c, Ni on 4b, Mn on 12d, and O (1) and O(2) oxygen ions occupy the 24e and 8c Wyckoff locations, respectively, make up the cation distribution in the P4332 symmetry. As a result, the unit cell volume is decreased due to a notable optimization of space occupation. It has been noted that the presence of impurities such NiO and/or LiyNi1-yO makes it challenging to synthesize phase-pure LNM. The partial In $LiNi_{0.5}$−y$Mn_{1.5}$−yCr_2yO_4, replacing Ni and Mn with Cr effectively addresses the issue of oxygen loss, which produces Mn3+ ions in the LNM framework and a voltage plateau at about 4 V vs. Li0/Li+. Therefore, it has been shown that Cr-doping lowers the energy density while stabilizing the lattice without appreciably affecting the capacity.

3.4. Olivine $LiFePO_4$ (LFP)

Numerous writers have examined the crystal structure of $LiFePO_4$ materials. LFP crystallizes in the orthorhombic system and belongs to the olivine family. It is composed of an oxygen framework that is deformed hexagonal close-packed (hcp) and contains Li and Half of the octahedral sites contain Fe ions, while one-eighth of the tetrahedral sites have P ions. However, the normal octahedral Oh is lowered to the Cs symmetry because to the distortion of the FeO_6 octahedra. The channels through which the lithium ions can be extracted are depicted in this structure in Figure 2. LiO_6 octahedra create edge-sharing chains along the b-axis, whereas corner-shared FeO6 octahedra are connected in the bc-plane. By sharing two edges with LiO_6 octahedra and one edge with one FeO6 octahedra, the tetrahedral PO4 groups connect adjacent layers of FeO_6 octahedra.

Three non-equivalent O sites make up the $LiFePO_4$ structure. With the exception of O(3), which occupies the general 8d position, and Li^+ ions, which only occupy the 4a Wyckoff position (M1 site on an inversion center), the majority of the atoms in the olivine structure occupy the 4c Wyckoff position. The magnetic ions of iron are in the divalent Fe2+ state and only occupy the center of the FeO_6 units, or the 4c Wyckoff position (M_2 site in a mirror plane). Consequently, Fe is dispersed in $TeOc_2$ layers perpendicular to the (001)-hexagonal directions, forming FeO_6 octahedra that are isolated from one another . Furthermore, a $TeOc_2$ layer is followed vertically by another one above it to create (100) layers of FeO_6 octahedra sharing corners and mixed layers of LiO_6, giving the lattice a significant two-dimensional character. octahedra and octahedra of PO_4. The principal mineral triphylite Li(Mn,Fe)PO_4 is different from the lithium iron phosphate substance in that triphylite is mostly rich in iron, with some manganese ions being present in the M_2 site . However, $LiFePO_4$ is an artificial product, whereas triphylite is a naturally occurring mineral.

Figure 3 displays the energy graphs vs. DOS indicating the relative Fermi level of the Li-insertion compounds covered in this section. LiCoO2's Co4+/3+ redox pair, the Ni4+/3+ redox $LiNi_{0.8}Co_{0.2}O_2$ couple, $LiMn_2O_4$ $Mn^{4+/3+}$ redox couple, and LiNiPO4 Ni3+/2+ redox couple. Additionally, the energies involved in the Li^+ and electron transfer define the cell voltage Voc. The idea of rechargeable lithium batteries is emphasized in the transfer. The crystal structure and coordination geometry of the site into/from which Li^+ ions are inserted/extracted define the energy involved in Li+ transfer, whereas the work functions of the cathode and anode are linked to the energy involved in electron transfer. To increase the cell voltage and energy density, the higher oxidation state must be stabilized. The higher valent states in oxides are accessible due to the placement of the O:2p energy and a greater raising of the Mn^+:d energies brought on by a larger Madelung energy. For this reason, positive electrode options for Li^- ion secondary batteries were investigated using transition-metal oxide hosts .

Figure 3: The relative Fermi level of the $Co^{4+/3+}$ redox pair for $LiCoO_2$, the $Ni^{4+/3+}$ redox couple for $LiNi_{0.8}Co_{0.2}O_2$, the $Mn^{4+/3+}$ redox couple for $LiMn_2O_4$, and the $Ni^{3+/2+}$ redox couple for $LiNiPO_4$ is displayed by comparing the energy vs. density of states.

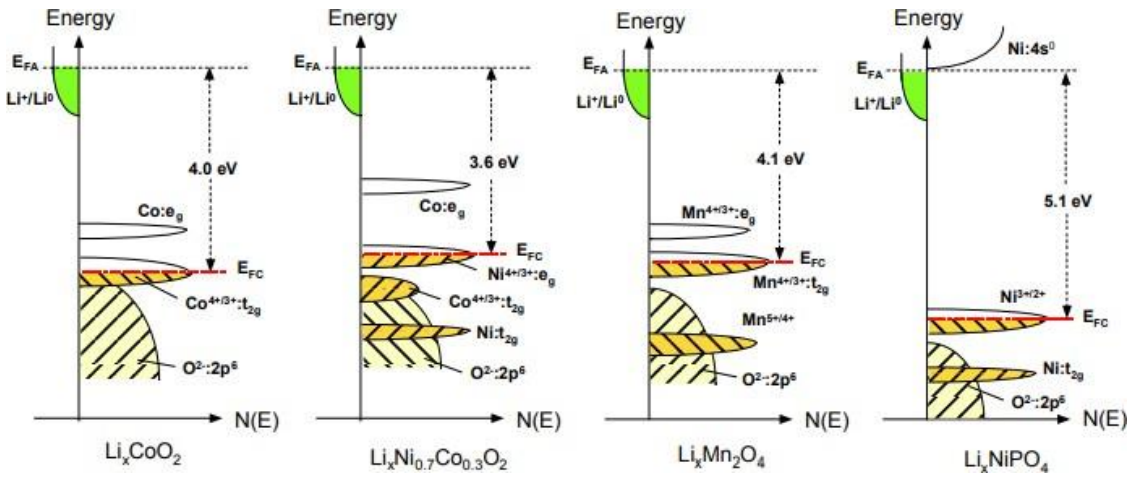

4. Electrochemical Properties and Phase Diagram

4.1. Lithium Cobaltate (LCO)

In LIBs, $LixCoO_2$ serves as the prototype positive electrode. Curves of charge and discharge $LixCoO_2$ in the range of 3.6–4.85 V versus. $Li0/Li^+$ at C/24 rate are displayed in Figure 4. As x fluctuates between 1.0 and 0.05, the order of the various phases is shown. Degradation and fatigue of LiCoO2 have been observed during electrochemical cycling. The shift can be understood as a shift in the orbital of the Co and oxygen wave functions as well as an increased energy overlap of the Co:3d and O:2p states. The DOS essentially stays the same for $1.0 \geq x \geq 0.5$, and the charge adjustment with Li extraction causes electrons to be removed from the Co:3d t2g derived states, causing the Fermi level to go downward (Figure 3). According to Laubach et al. [33], the valence band (VB) remains mostly unaltered with a minor shift at the top of the VB toward lower binding energies. This suggests a shift in EFC that causes the d-electrons to be removed as a result of the oxidation state changing from Co^{3+} to $Co^{4+.}$ For $x < 0.5$, a noticeable rise The reduction of the c-axis lattice parameter indicates that hybridization between the Co:3d and O:2p states is linked to a decrease in the (CoO_6)-slab distances. Consequently, the A partial oxidation of the $O2-$ ions results from the removal of electrons from Co-O:d-p hybrid states caused by charge compensation of the delithiation .

Figure 4: Curves of charge and discharge $LixCoO_2$ in the range of 3.6–4.85 V versus. $Li0/Li^+$ at C/24 rate . As x fluctuates between 1.0 and 0.05, the order of the various phases is shown.

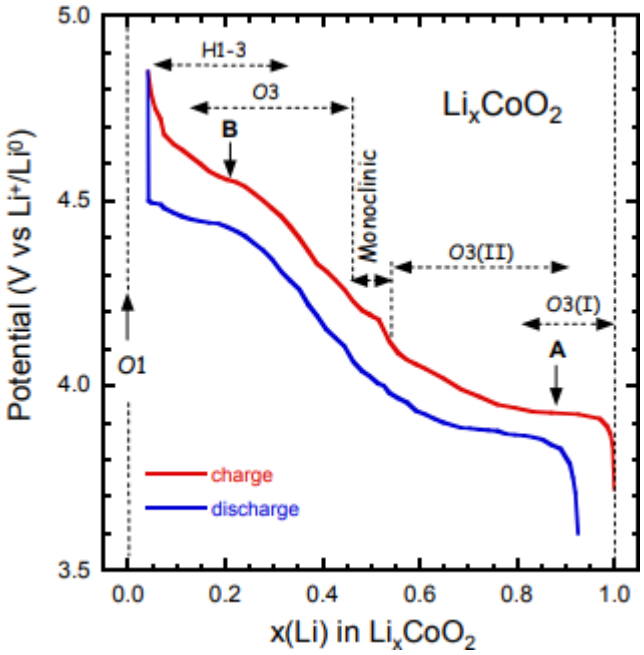

4.2. Lithium Manganese Spinel (LMO)

Manganese is abundant in nature and five times less expensive than cobalt. The spinel $LiMn_2O_4$ shows good structural stability during the charge-discharge process and possesses a robust edge-

shared $[Mn_2]O_4$ octahedral lattice. $LiMn_2O_4$ spinels have demonstrated a lack of cycle robustness. life and irreversible capacity loss, which accelerates at high temperatures . Li+ ions are removed from the tetrahedral sites of the $LixMn_2O_4$ spinel structure at about 4 V in a two-stage procedure, separated by about 150 mV, according to the electrochemical data. at a $Li_{0.5}Mn_2O_4$ composition (Figure 5). The λ-MnO_2 phase, or λ-γ$[Mn_2]O_4$ in the spinel nomenclature, forms at x = 0. The arrangement of the lithium ions on one side of the tetrahedral 8a sites is what causes the two-step process. The 3-D 8a-16c-8a-16c network offers an energetically favorable pathway for the quick diffusion of lithium in and out of the structure during discharge and charge, respectively. Li typically travels from the tetrahedral 8a site to the unoccupied octahedral 16c site in the spinel LMO.

About 3 V is when lithium is inserted into the LMO. Li+ ions are introduced into the spinel structure's octahedral 16c locations during this procedure. Given that the 16c and 8a octahedra have faces in common, Li+ ions on tetrahedra are immediately displaced into nearby vacant 16c octahedral sites due to electrostatic interactions between the Li+ ions on these two sets of sites. On the surface of the electrode particle, the reaction produces a first-order transition to Li2Mn2O4 with a stoichiometric rock-salt composition. Thus, at 3 V, the electrochemical process is a two-phase reaction. A $Li_2Mn_2O_4$ reaction front gradually advances from the particle's surface into the bulk during discharge. Due to an elevated concentration of Mn3+:d4 ions in the Mn2O4 spine1 lattice, the Li insertion is accompanied by a significant Jahn-Teller distortion at 3 V, which lowers the crystal symmetry from cubic (c/a = 1.0) to tetragonal (c/a = 1.16), which causes the c/a ratio to rise by 16% and is harmful to electrochemical cycling.

Figure 5: Li//LiMn2O4 cell voltage profile discharged at C/24 rate using 700 °C-synthesised LMO material (left). Lattice parameter variation during charge/discharge in an LMO cathode as a function of Li concentration x (right).

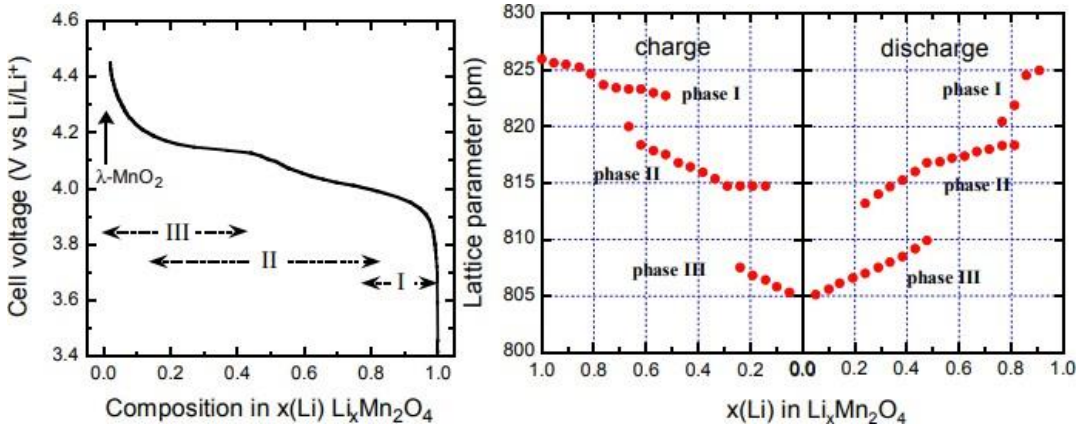

A two-phase structure coexists in the high-voltage area for LMO and endures throughout Li-ion insertion/extraction at low temperatures during cycling, using in situ X-ray diffraction. A mathematical model for an LMO's capacity fading. electrode by taking into account the solid

electrolyte interphase (SEI) film development on the surface of the LMO particles and the acid attack on the active material. The Mn dissolution is combined with the acid produced by the $LiPF_6$ and solvent breakdowns. Another factor contributing to the capacity fade, which is brought on by the passive film generation on the surface of the active material, is the decrease in the Li ion diffusion coefficient.

The capacity reduction of Li//$LixMn_2O_4$ cells in the 4-V area has been attributed to a number of factors, including the following .

(i) The primary disadvantage is the disproportionation of Mn^{3+} into Mn^{2+} and Mn^{4+} at the particle surface when trace amounts of protons are present (acid attack).

$$2Mn^{3+}_{(solid)} \rightarrow Mn^{4+}_{(solid)} + Mn^{2+}_{(solution)} \quad (3)$$

causing Mn^{2+} ions to leak into the electrolyte from the positive electrode structure . According to Xia et al. , chemical analysis data showed that only 23% and 34% of the total capacity losses cycling at the time were due to the simple dissolving of Mn^{3+}. 50 °C and room temperature, respectively. Surface coating of the particles with a thin layer of inorganic material, such as Al_2O_3 , zirconia, MgO , Li_2O-B_2O_3 glass , AlF3 , etc., is the proper technique to lessen capacity fading of LMO. Surface treatment is a useful technique for enhancing LMN spinals' capacity to store high temperatures. This has been accomplished by establishing a barrier layer of protection surface demonstrating how crucial it is to regulate the surface chemistry. Selecting a chemical composition that keeps Mn inactive in the 4+ valence state has been another method of avoiding this issue; this is the case for $LiNi_{1/3}Mn_{1/3}Co_{1/3}O_2$ and $LiNi_{1/2}Mn_{3/2}O_4$.

(ii) At the end of the charge, oxygen loss in organic electrolyte solvents causes instability of the delithiated spinel structure.

(iii) The beginning, especially at high current density, of a Jahn-Teller effect at the conclusion of discharge. It has been suggested that certain crystallites may be more lithiated than others under dynamic, non-equilibrium conditions over 3 V, which would cause the electrode surface's composition to shift toward a Mn3+-rich area of $Li1+xMn_2O_4$.

Furthermore, spinel $LiMn_2O_4$ has a specific capacity of less than 120 $mAhg^{-1}$ at 4.1 V vs. Li0. /Li^+, meaning that 0.8 Li is extracted for every unit of formula. It has also been noted that at a potential of about 3 V vs. Li0/Li^+, more Li could be added to the spinel framework's empty octahedral holes. This would result in a structural shift from cubic to tetragonal symmetry because of the Jahn-Teller distortion connected to the high-spin Mn^{3+} (t2g 3 eg 1) ions, which would cause a significant volume change and capacity fade. High-resolution electron diffraction and imaging have shown evidence of structural fatigue at the surface of discharged $LixMn_2O_4$ spinel electrodes in Li//$LixMn_2O_4$ cells. Even at 500 mV above the voltage anticipated for the start of the tetragonal phase, domains of tetragonal $Li_2Mn_2O_4$ coexist with cubic $LiMn_2O_4$ under non-equilibrium conditions. $Li_2Mn_2O_4$ on the particle surface could be a factor in the capacity fade. noticed during Li//$LixMn_2O_4$ cell cycling, as a result of the loss of particle-to-particle

contact at the discharge state's cubic-$_{LiMn2O4}$/tetragonal- Li//$LixMn_2O_4$ $Li_2Mn_2O_4$ interface. $LixMn_2O_4$ ($0 \leq x \leq 1$) cathode materials have been studied using in situ XRD during Li+ ion extraction and insertion.

The initial charge-discharge cycle in the 4-V area exhibits three-phase behavior (Figure 5). Two plateaus in the voltage profile, located at 4.05 and 4.15 V, are indicative of two-phase systems that are induced by three cubic phases. $LiMn_2O_4$ is an electrical small-polaron semiconductor. conduction through electron hopping between neighboring Mn3+/Mn4+ cations, for example. Therefore, the quantity of mobile electrons throughout the entire solid should decrease as a result of the slow removal of Li+ ions from the lattice during de intercalation .

4.3. Lithium Mn-Ni-Co Oxides

The hexagonal single-phase α-$NaFeO_2$-type layered LiNiyMnyCo1−2yO2 (NMC) compounds have drawn a lot of interest as 4V-electrode materials to replace LiCoO2 in Li-ion batteries because of its improved cycling stability even at high temperatures, larger reversible capacity, and reduced heat stability when in a charged condition [51]. Its reversible capacity was measured to be 200 mAh g−1 in the 2.8–4.6 V cut-off range and 160 mAh g−1 in the 2.5–4.4 V cut-off range . Since the ionic radius of Li+ (0.76 Å) is near to that of Ni2+ (0.69 Å), the primary issue that remains unresolved for such NMC applications is the cation mixing between nickel and lithium ions. It is well known that the cation mixing of Li+ and Ni2+ ions on the NMC lattice's crystallographic (3b) sites degrades their performance of electrochemistry. The structural model [Li1−δNiδ]3b[LiδNix−δMnyCo1−x−y]3aO2 has been shown to be valid by Rietveld refinement of the XRD data (see detail in ref. [53]). The NMC electrodes are more stable than the LCO electrodes in the 2.8–4.6 V potential region, according to a rigid-band model that calculates the relative positions of the Fermi level and the O:2p band with respect to the Ni4+/3+ and Co4+/3+ redox couples for $LiNiyMnyCo1-2yO_2$ as a function of x(Li) during the charge (Figure 6).

4.4. LMN and Doped-LMN Electrodes

A method to greatly enhance the electrochemical cycling of $LiMn_2O_4$ materials is to partially substitute metal cations for the Mn in the $LiMn_2-yMyO_4$ and $LiMn_{1.5}-yNi_{0.5}-yM2yO_4$ solid solutions (where M = Ni, Cu, and Cr), but at the cost of a reduction in the initial capacity. below 4.4 V, which is the useful voltage window. The reason for this good outcome is the decrease in Mn3+ JT ion concentration, which triggers the tetragonal phase transition in the 3-V zone. For instance, cyclic voltammetry experiments in the early work of Ein-Eli and Howard [54] demonstrated that Cu substitution for Mn in LMO displayed two discharge regimes, at 4.1 and 4.9 V vs. the Li0 Li+ couple. LiCux IICuy IIIMn[2−(x+y)] III,IVO4 had a discharge capacity of 71 mAh g−1 (97% theoretical). According to investigations, the composition LMN has particular electrochemical properties, including a high capacity of 130–140 $mAhg^{-1}$ linked to a high-voltage plateau at 4.7 V .

Figure 6: The relative Fermi level of the $Ni^{4+/3+}$ and $Co^{4+/3+}$ redox couples for $LixNiyMnyCo1-2yO_2$ during the charge is displayed by the energy vs. density of states for three charge states that are governed by the Li concentration x: (a) x = 1; (b) x = 0.5; and (c) x = 0.

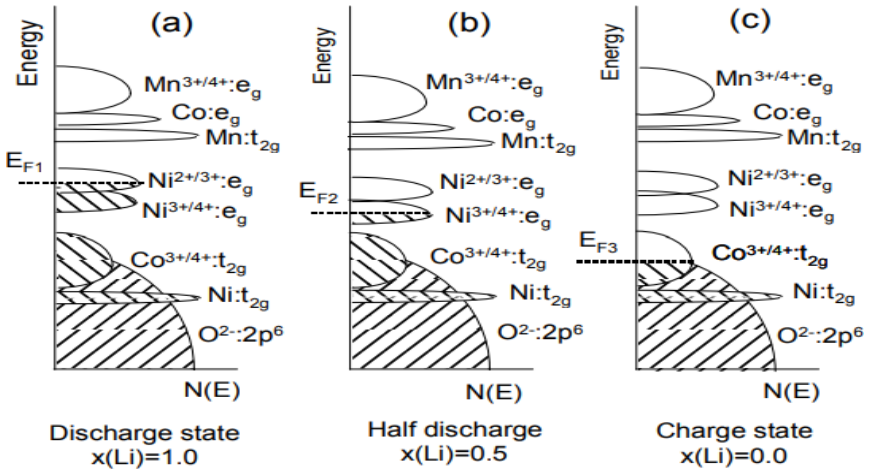

Due to oxygen loss during high-temperature production, the distinctive 4.1 V Mn3+/4+ redox pair is consistently seen in the pristine or metal-doped LMN electrodes, according to the electrochemical characteristics. But in $LiMn_{1.45}Ni_{0.45}Cr_{0.1}O_4$ spinel, no discernible 4.1 V step is found, indicating that inn accordance with the magnetic property analysis, the majority of the remaining Mn^{3+} ions were re-oxidized to Mn4+ upon re-annealing at 600 °C [26]. Additionally, this aligns with the findings of the Rietveld refinement. Figure 7 contrasts the incremental capacity curves, dQ/dV vs. V plots, to help visualize the variations in the electrochemical characteristics of various electrode materials. When Li is removed from the spinel LMN framework's tetrahedral sites, the oxidation reaction of Ni2+/3+ is first probed immediately below 4.7 V (usually ~4.69 V) for the disordered Fd3m and above 4.7 V (usually ~4.72 V) for the P4332 spinels that are arranged [56]. The V(x) profile of LMN is raised by around 0.02 eV when the Ni and Mn are ordered. For the Cr-doped LMN, Figure 7 shows two anodic peaks at 4.663 and 4.731 V along with two cathodic peaks at 4.638 and 4.704 V. These values are consistent with two voltage plateaus for disordered LMN. According to Kim et al., the voltage gaps between the two plateaus narrowed at about 4.75 V as the crystallographic structure changed from Fd3m to P4332, producing a flatter voltage profile .

4.5. Lithium Iron Phosphate ($LiFePO_4$)

The phospho-olivine $LiFePO_4$ (LFP) is regarded as a promising positive electrode material for use in lithium rechargeable batteries, with a theoretical specific capacity of 170 mAhg−1 at moderate current densities cells; it has two key advantages over cobalt-oxide-based materials for

large-scale applications like hybrid electric vehicles (HEVs): it is affordable and non-toxic. However, during high-rate discharging, capacity losses could occur because to LFP's poor electronic conductivity (σe < 10−9 S cm^{-1}) and low Li^+ ion diffusion coefficient (D ~ ≈ 10−14 cm2 s^{-1}). On the other hand, brief Li^+-ion diffusion pathways within the positive electrode are made possible by the reduction of the LFP particles to the nano size. Furthermore, the production of LFP coated with carbon significantly improves electrical conduction between particles, guaranteeing high rate capability and avoiding particle aggregation.

The redox potential of ($Fe^{2+}/Fe^{3+)}$ at approximately 3.45 V vs. Li0/Li+ is obtained by electrochemically extracting Li from LiFePO4. A flat V-x curve and a two-phase separation spanning the majority of the solid-solution range 0 < x < l for LixFePO4 are the results of a minor but first-order displacive structural modification of the framework. The carbon-coated nanostructured cathode particles provide a reversible capacity of about 160 $mAhg^{-1}$. The high caliber of the "optimized" $LiFePO_4$—impurity-free materials utilized as positive electrodes—is responsible for this outcome. The voltage profiles of $LiFePO_4$//Li cells are shown in Figure 8a as a function of the electrode material preparation. These graphs demonstrate that the specific capacity is less than 100 mAh g^{-1} in the absence of carbon coating, whereas a 3-nm thick carbon film put atop 500-nm sized LFP particle increases the discharge capacity at C/12 rate to 141 mAh g^{-1} .

Figure 7: dQ/dV vs. V differential capacity curves for the (a) LMN and (b) Cr-doped LMN. Volt is used to express the values at the peaks .

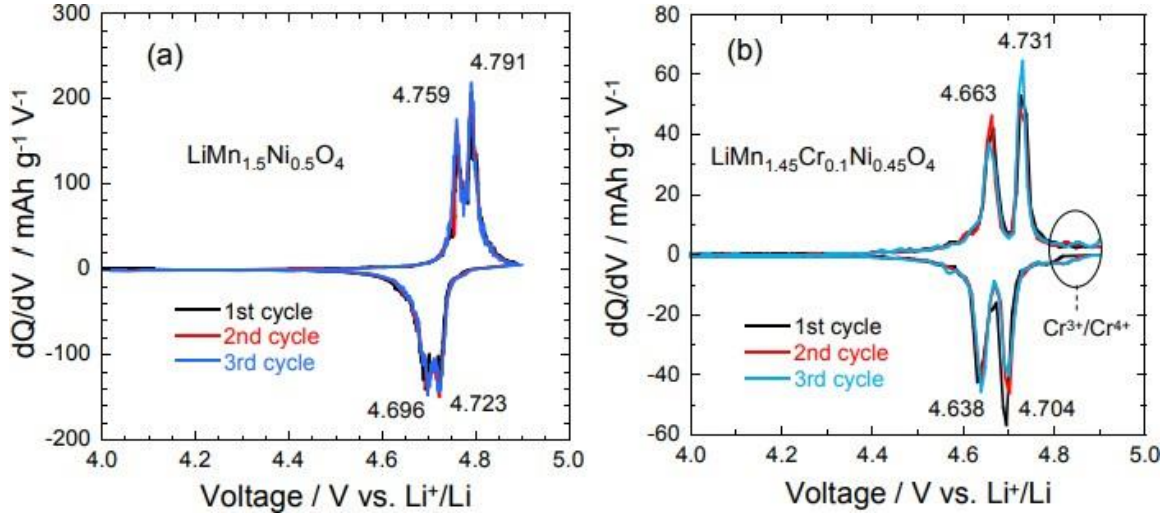

Using the same standard electrolyte, 1 mol L−1 $LiPF_6$, the electrochemical performance of optimized LFP and LTO electrode materials has been evaluated independently in half cells with regard to Li metal anode. in diethylene and ethylene carbonates (EC and DEC) . Together with the potential-capacity curve of the LTO//LFP lithium-ion battery, the voltage vs. capacity curves

obtained under such circumstances at 25 °C are shown in Figure 8b at low C-rate C/24 to approach thermodynamic equilibrium battery. For $LiFePO_4$, the voltage window is 2–4 V, whereas for $Li_4Ti_5O_{12}$, it is 1.2–2.5 V. Please take note that we have adhered to the standard practice in this figure (and the ones that follow), which states that the capacity is expressed in mAh per gram of the cathode's active element. This explains why the LFP//Li and LFP//LTO cells have the same maximal capacity. LFP//Li has a reversible capacity of 148 mAh g−1 and a first coulombic efficiency of 100%. LTO has a reversible capacity of 157 mAh g-1 and a first coulombic efficiency of 98%. The topotactic insertion/deinsertion of lithium in the two-phase systems $LiFePO_4$-$FePO_4$ and $Li_4Ti_5O_{12}$-$Li_7Ti_5O_{12}$ is characterized by the well-known plateaus at 3.4 and 1.55 V, respectively .

Figure 8: (a) Before and after carbon coating, the LiFePO4//Li coin cell's electrochemical performance at room temperature. At the C/12 rate, charge-discharge cycling was carried out. **(b)** $LiFePO_4$//Li, $Li_4Ti_5O_{12}$-$Li_7Ti_5O_{12}$ //Li, and Li-ion cell voltage-capacity cycle C/24 rate of $LiFePO_4$// $Li_4Ti_5O_{12}$-$Li_7Ti_5O_{12}$ [62]. The capacity is expressed in milliamperes per gram of the LiFePO4, Li4Ti5O12, and LiFePO4 positive electrode elements, respectively. Although the plateau at 1.9 V is clearly visible, the $LiFePO_4$// $Li_4Ti_5O_{12}$-$Li_7Ti_5O_{12}$ cell's higher hysteresis results from the fact that it was a button cell rather than the more complex 18650-cell. One mol L^{-1} $LiPF_6$ in EC:DEC (1:1) was utilized as the electrolyte in each cell.

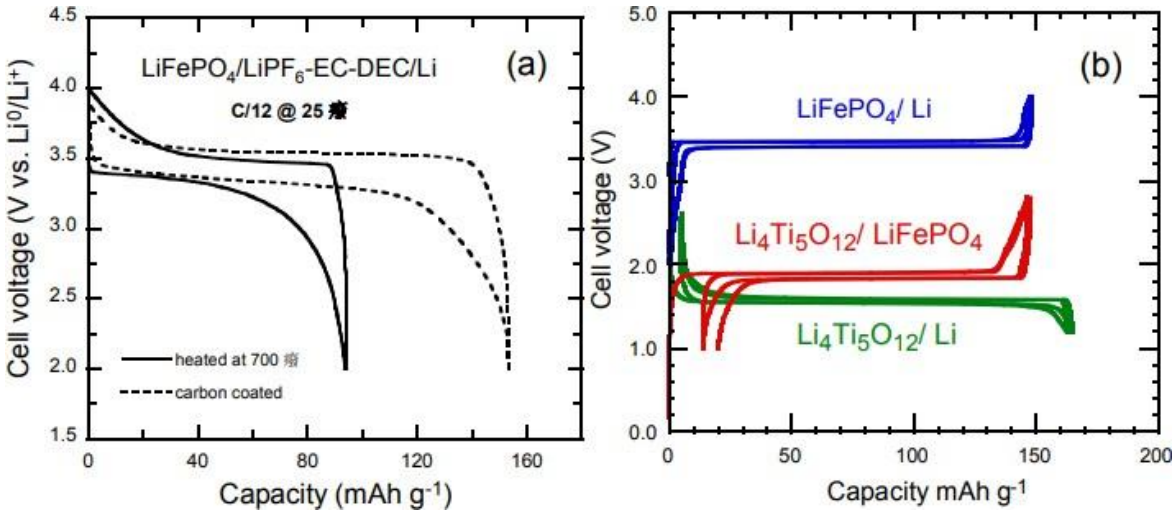

5. Safety Issues

5.1. Loss of Oxygen in $LixCoO_2$

Since the $LixCoO_2$ cathodes are known to cycle successfully for $x > 0.5$, electrochemical cells may not experience any oxygen loss. A quicker and deeper extraction of lithium on the surface may be the cause of the observed onset of oxygen loss at a somewhat higher Li content $x = 0.45$, though Since the average lithium level is greater than 0.5, the overall oxygen content may be somewhat below 2 for $0.5 \leq x \leq 0.45$. Because the Co4+/3+:t2g band overlaps with the O:2p

orbitals, the band diagrams in Figure 9 illustrate the variations in chemical instability with regard to oxygen loss.

Oxygen loss occurs below lithium content x = 0.5, according to chemical analysis of electrochemically charged $Li1-xCoO_2$ samples . The findings imply that the cobalt oxide system in Li-ion cells is inherently vulnerable to oxygen loss for x < 0.5. The lattice's loss of oxygen in Capacity fade may be caused by the $Li1-xCoO_2$ system, which has a restricted capacity of 140 $mAhg^{-1}$. However, a larger capacity of about 180 mA g^{-1} can be realized due to the $Li_xNi_{0.85}Co_{0.15}O_2$ system's lack of oxygen loss for $0.7 \leq x \leq 0$ and the presence of the second phase at a significantly lower lithium concentration x < 0.77.

5.2. Comparative Safety Issues

Thermal stability for lithium-insertion compounds use as positive electrodes in Li-ion batteries has been studied for C-$LiFePO_4$, $LiNi_{0.8}Co_{0.15}Al_{0.05}O_2$, $LiNi_{0.33}Co_{0.33}Mn0.33O_2$ and $LiCoO_2$ [66].Figure 10 shows differential scanning calorimetry (DSC) spectra of the overcharged spinel ($LiMn_2O_4$), layered ($LiNi_{0.8}Co_{0.15}Al_{0.05}O_2$) cathode and carbon-coated $LiFePO_4$, all electrodes with traces of 1.2 mol L^{-1} $LiPF_6$ in ethylene carbonate:ethyl-methyl carbonate (3:7), measured at a scan rate of 10 °C min^{-1} from 50–400 °C. We can observe that both spinel and olivine cathodes have delayed onset temperature by at least 70 °C with respect to the layered cathode. The DSC results for layered, spinel, and olivine positive electrodes are summarized in Table 2. The layered cathode was determined to be thermally unsafe because it undergoes its exothermic reaction with a very large enthalpy (−941 Jg^{-1}) and the reaction is completed at a much earlier temperature, lower than the onset temperature of spinel and olivine. The spinel cathode showed about half the exothermic reaction enthalpy (−439 Jg^{-1}), while carbon-coated olivine showed even lower exothermic reaction enthalpy (−250 Jg^{-1}).

Figure 9: $LixCoO_2$'s qualitative energy diagrams change in response to the amount of lithium present. x = 1, x = 0.5, and x = 0 are in order from left to right.

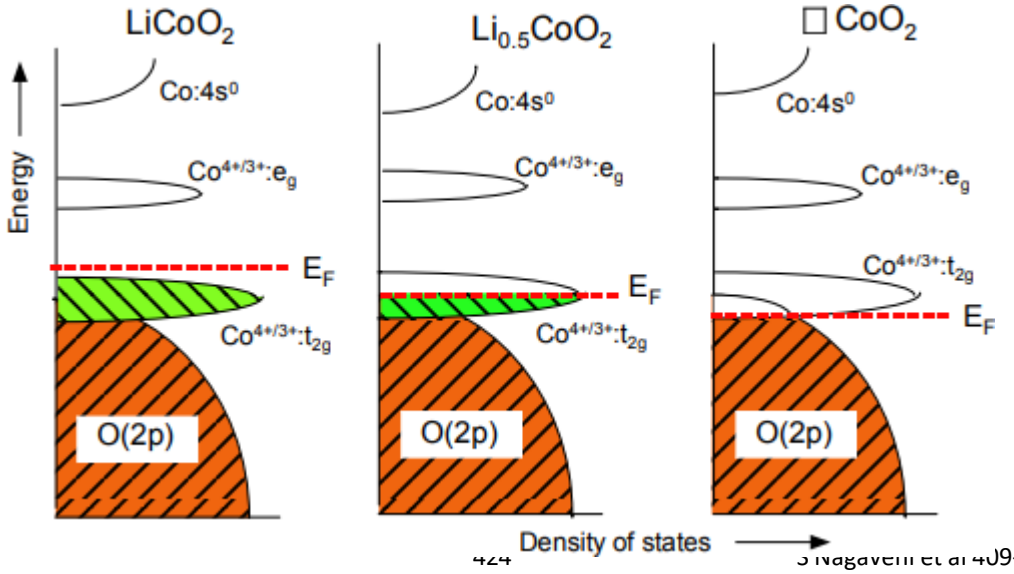

step 1: $LixNi_{0.8}Co_{0}.15Al_{0.05}O_2$ undergoes partial structural deformation into disorder in the first stage. oxide (spinel-like structure), and as a result of this structural deformation, a tiny quantity of oxygen is released from it. Step 2: Because of its lower flash point of 150 °C, this step involves the reaction of the oxygen generated in Step (1) with the ethylene carbonate.

$$C_3H_4O_3 + 2.5O_2 \rightarrow 3CO_2 + 2H_2O \quad (4)$$

The system's temperature rises as a result of the oxygen's ongoing reaction with EC and potentially EMC, which generates combustion heat. Step (3): The heat generated in the aforementioned reaction speeds up the structural deformation even more, ultimately resulting in the oxide's total structural collapse.

$$Li_{0}.36Ni_{0}.8Co0.15Al_{0}.05O_2 \rightarrow 0.18Li_2O + 0.8\ NiO + 0.05Co_3O_4 + 0.025Al_2O_3 + 0.372O_2 \quad (5)$$

Finally, Step (4): The aforementioned process generates a significant quantity of heat and oxygen, which aids in the thermal runaway caused by the burning of the residual electrolyte (EC, EMC, and LiPF6).

$$C_3H_4O_3 + 2.5O_2 \rightarrow 3CO_2 + 2H_2O \quad (6)$$

$$C_3H_8O3 + 2.5O_2 \rightarrow 3CO_2 + 2H_2O \quad (7)$$

In contrast, the phase transition to FePO4 in LiFePO4 is thought to happen in Step (1) as opposed to the structural disordering seen in a layered cathode. While Step (3) is mostly avoided due to the heat emitted from the combustion of the multilayer cathode, Step (2) is seen to the same degree. The $LiFePO_4/FePO_4$ cathode's structural stability results from the use of solvents containing O_2 to preserve the $FePO_4$ phase. Once more, $LiFePO_4$'s $(PO_4)_{3-}$ polyanion's strong P-O covalent connections dramatically lower the rate of O2 release, which lowers the combustion step and prevents more cathode structural damage.

Figure 10. DSC spectra of olivine, spinel, and overcharged layered cathodes in EC-EMC (3:7) electrolyte at 10 °C min−1 with traces of 1.2 mol L−1 $LiPF_6$.

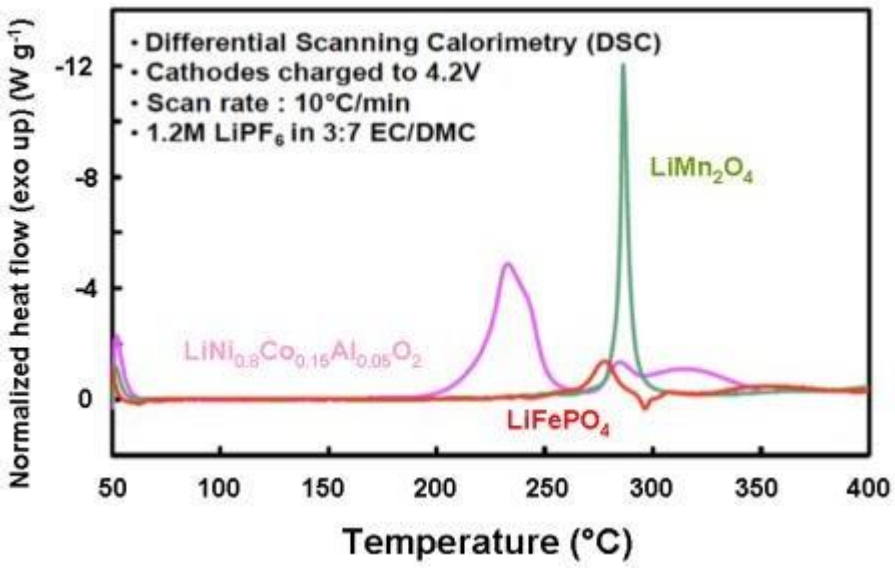

Table 2. The three last columns report the flow of enthalpy inferred from the DSC spectra of the fully lithiated carbon-coated graphite and the fully delithiated and overcharged carbon-coated LiFePO4 of the overcharged cathode elements under investigation.

Cathode material	Onset T (°C)	Overall ΔH (J g^{-1})
$LiNi_{0.8}Co_{0.15}Al_{0.05}O_2$	170	−941
$LiMn_2O_4$	264	−439
$LiFePO_4$	245	−250

$LiFePO_4$'s cell temperature is elevated to no more than 34 °C during charge and discharge at a 0.5C rate, according to isothermal micro-calorimetry (IMC) studies, while DSC measurements revealed that $LiFePO_4$ is less reactive with electrolyte at high temperatures than spinel. and cathodes that are stacked. Furthermore, it was shown that the disintegration of the SEI layer caused fully lithiated graphite to exhibit greater exothermic heat than the $LiFePO_4$ cathode itself. In order to determine the total combination of exothermic reaction temperatures of $LiFePO_4$, graphite, and electrolyte, a fully charged cylindrical 18,650 cell employing $LiFePO_4$/graphite was evaluated in an Accelerating Rate Calorimeter (ARC) . Figure 11 reports the in-situ cell open-circuit potential, heater temperature, and simultaneous cell temperature that were obtained during the cell's ARC test. It demonstrates that the cell received consistent heating as Throughout the experiment, the thermocouples on the heater's top, side, and base all showed the same temperature, and the cell temperature closely matched the heater temperature until any self-heat was released. Throughout this time, the open-circuit potential was steady at about 3.3 V. Additionally, open-circuit potential started to progressively decrease as a result of the resistive heating of the cell. Following 1455 minutes of testing, the open-circuit potential started to rapidly decrease and the cell temperature started to climb sharply to 150 °C. The cell's internal short circuit caused by the separator melting was the reason given for this behavior. The cell

fully broke down and the temperature of the cell exploded away from the heater temperature by over 80 °C at 1756 minutes of testing. A few minutes later, the cell voltage suddenly dropped to almost zero.

Figure 11: LiFePO4/C 18,650 cells were subjected to an ARC test, and the in-situ open-circuit potential was recorded chronologically. The cell temperature was measured at the heater's base, top, and side (the curves are superimposed).

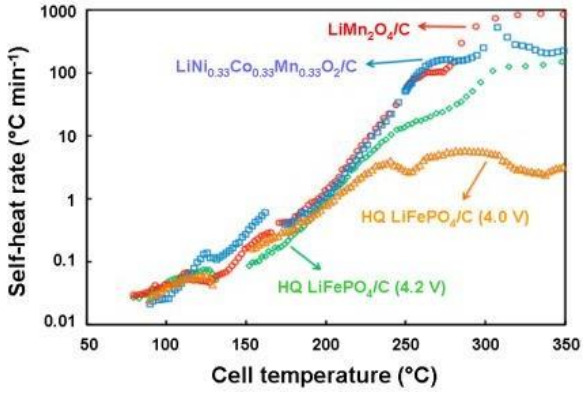

6. Concluding Remarks

The following factors should be taken into account while developing appropriate hosts with compatible anodes for the next generation of Li-ion cells for electric or portable electronic vehicles: structural and chemical stability, electrode capacity, voltage, rate capability, and service thermal and life safety. Eliminating undesired chemical interactions between the electrolyte and electrode materials is necessary for a long service life. The active electrode material's strong capacity retention across a large number of charge-discharge cycles limits the volume change in relation to its state of charge. The electrolyte's flammability, the charge and/or discharge rate, and structural stability—that is, the lack of oxygen created by the cathode's structural collapse—all affect safety.

References

1. Maleki Kheimeh Sari, Hirbod, and Xifei Li. "Controllable cathode–electrolyte interface of Li [Ni0. 8Co0. 1Mn0. 1] O2 for lithium ion batteries: a review." *Advanced Energy Materials* 9.39 (2019): 1901597.
2. Feng, Xuning, et al. "Thermal runaway mechanism of lithium ion battery for electric vehicles: A review." *Energy storage materials* 10 (2018): 246-267.
3. Reyes, Christopher, et al. "Three-dimensional printing of a complete lithium ion battery

with fused filament fabrication." *ACS Applied Energy Materials* 1.10 (2018): 5268-5279.

4. Pramudita, James C., et al. "An initial review of the status of electrode materials for potassium-ion batteries." *Advanced energy materials* 7.24 (2017): 1602911.
5. Berckmans, Gert, et al. "Cost projection of state of the art lithium-ion batteries for electric vehicles up to 2030." *Energies* 10.9 (2017): 1314.
6. Dixit, Mudit, et al. "Origin of structural degradation during cycling and low thermal stability of Ni-rich layered transition metal-based electrode materials." *The journal of physical chemistry C* 121.41 (2017): 22628-22636.
7. Massé, Robert C., et al. "Energy storage through intercalation reactions: electrodes for rechargeable batteries." National Science Review 4.1 (2017): 26-53.
8. Blomgren, George E. "The development and future of lithium ion batteries." *Journal of The Electrochemical Society* 164.1 (2016): A5019.
9. Haregewoin, Atetegeb Meazah, Aselefech Sorsa Wotango, and Bing-Joe Hwang. "Electrolyte additives for lithium ion battery electrodes: progress and perspectives." *Energy & Environmental Science* 9.6 (2016): 1955-1988.
10. Julien, Christian, et al. *Lithium batteries*. Springer International Publishing, 2016.
11. Andre, Dave, et al. "Future generations of cathode materials: an automotive industry perspective." *Journal of Materials Chemistry A* 3.13 (2015): 6709-6732.
12. Meshram, Pratima, B. D. Pandey, and T. R. Mankhand. "Recovery of valuable metals from cathodic active material of spent lithium ion batteries: Leaching and kinetic aspects." *Waste management* 45 (2015): 306-313.
13. Hong, Jihyun, et al. "Lithium-excess layered cathodes for lithium rechargeable batteries." Journal of The Electrochemical Society 162.14 (2015): A2447.
14. Wang, Jiajun, et al. "Surface aging at olivine LiFePO 4: a direct visual observation of iron dissolution and the protection role of nano-carbon coating." Journal of Materials Chemistry A 1.5 (2013): 1579-1586.
15. Julien, Christian M., et al. "Enhanced electrochemical properties of LiFePO 4 as positive electrode of Li-ion batteries for HEV application." (2012).
16. Zhang, Xiaoyu, et al. "Minimization of the cation mixing in Li1+ x (NMC) 1− xO2 as cathode material." Journal of Power Sources 195.5 (2010): 1292-1301.
17. Myung, Seung-Taek, Jongsoon Kim, and Yang-Kook Sun. "Anticipated Progress in the Near-to Mid-Term Future of LIBs." *Encyclopedia of Electrochemistry: Online* (2007): 1-32.